Nano Research 2016, 9(5): 1460–1469
DOI 10.1007/s12274-016-1042-9
Research Article
ISSN 1998-0124
CN 11-5974/O4

Precise synthesis of discrete and dispersible carbon-protected magnetic nanoparticles for efficient magnetic resonance imaging and photothermal therapy

An-Hui Lu[1] (✉), Xiang-Qian Zhang[1], Qiang Sun[1], Yan Zhang[2] (✉), Qingwei Song[2], Ferdi Schüth[3] (✉) Chunying Chen[4], and Fang Cheng[5]

[1] *State Key Laboratory of Fine Chemicals, School of Chemical Engineering, Faculty of Chemical, Environmental and Biological Science and Technology, Dalian University of Technology, Dalian 116024, China*
[2] *Dalian Medical University affiliated No.1 Hospital, Dalian 116021, China*
[3] *Max-Planck-Institut für Kohlenforschung, Kaiser-Wilhelm-Platz 1, D-45470 Mülheim an der Ruhr, Germany*
[4] *CAS Key Laboratory for Biomedical Effects of Nanomaterials and Nanosafety, National Center for Nanoscience and Technology of China and Institute of High Energy Physics, Chinese Academy of Sciences, Beijing 100190, China*
[5] *State Key Laboratory of Fine Chemicals, School of Pharmaceutical Science and Technology, Dalian University of Technology, Dalian 116024, China*

Received: 11 December 2015
Revised: 29 January 2016
Accepted: 3 February 2016

KEYWORDS

magnetic nanoparticles, carbon, Fe_3O_4, magnetic resonance imaging (MRI), colloidal suspensions, photothermal therapy

ABSTRACT

Carbon-protected magnetic nanoparticles exhibit long-term stability in acid or alkaline medium, good biocompatibility, and high saturation magnetization. As a result, they hold great promise for magnetic resonance imaging, photothermal therapy, etc. However, since pyrolysis, which is often required to convert the carbon precursors to carbon, typically leads to coalescence of the nanoparticles, the obtained carbon-protected magnetic nanoparticles are usually sintered as a non-dispersible aggregation. We have successfully synthesized discrete, dispersible, and uniform carbon-protected magnetic nanoparticles via a precise surface/interface nano-engineering approach. Remarkably, the nanoparticles possess excellent water-dispersibility, biocompatibility, a high T_2 relaxivity coefficient (384 $mM^{-1}·s^{-1}$), and a high photothermal heating effect. Furthermore, they can be used as multifunctional core components suited for future extended investigation in early diagnosis, detection and therapy, catalysis, separation, and magnetism.

Address correspondence to An-Hui Lu, anhuilu@dlut.edu.cn; Yan Zhang, zhangyanmed@126.com; Ferdi Schüth, schueth@mpi-muelheim.mpg.de

1 Introduction

Magnetic nanoparticles have great potential in applications like bioseparation, magnetic resonance imaging, magnetic fluids, and catalysis. [1–6]. Uniform, water dispersible, magnetic nanoparticles with excellent stability are highly desirable for *in vivo* clinical imaging and other biomedical applications. So far, a number of magnetic nanoparticles with different compositions and shapes have been developed [7–12]. However, naked magnetic nanoparticles tend to aggregate and are easily oxidized in air, leading to uncontrolled magnetic behavior and losses in magnetism and dispersibility [13–16]. Different protection strategies have been proposed to overcome these problems, such as grafting or coating organic or inorganic materials including surfactants or polymers [17–21], silica [22–26], carbon [27–29], etc. However, most of them are not stable in the application environments (e.g., corrosive or basic solutions or organic solvents), especially for bio-related applications where dispersibility and biocompatibility of the protected nanoparticles cannot meet the requirements due to incorrect coating strategies or the nature of the coating materials. It is thus crucial to develop other protection strategies that not only stabilize core magnetic nanoparticles against harsh media, but also improve their dispersibility and biocompatibility *in situ* [13, 25, 30].

Carbon is an excellent coating material since it is biocompatible and stable over the entire pH range and is easily functionalized [31, 32]. Carbon has been used as a scaffold for nano-architectures including hollow structures, core–shell, and sandwich or lamellar heterostructures, all aimed at achieving multifunctionality [27–29, 33–35]. A hindrance in using carbon-coated nanostructures is to achieve good dispersibility by overcoming the nature of carbon, which is to coalesce during pyrolysis. In our previous work, a confined pyrolysis method [36] was developed to prepare discrete hollow carbon spheres, in which an inorganic outer silica layer was coated on the carbon precursor, creating a confined nanoreactor to prevent the coalescence of nanocarbons during the high-temperature treatment.

Inspired by this work, in this study, we have demonstrated an accurately controlled surface/interface nano-synthesis strategy for the preparation of carbon-protected Fe_3O_4 (Fe_3O_4@C) magnetic nanoparticles. The obtained Fe_3O_4@C nanoparticles have several advantages. First, the nanoparticles are monodispersive in water without clustering and aggregation. Further, they possess high biocompatibility, which is mandatory for their biomedical and magnetic applications. The second notable characteristic is their high magnetization of 90 $emu \cdot g^{-1}$ (normalized to the Fe_3O_4 content), which enables these nanoparticles for magnetic resonance imaging (MRI) contrast enhancement and other biological separations. Remarkably, the sample showed a high T_2 relaxivity coefficient (r_2) of 384 $mM^{-1} \cdot S^{-1}$, demonstrating strong potential for applications such as cancer treatment by combining the high photothermal heating effect of this material. This precise hybridization of monodispersed, uniform carbon-coated magnetic nanoparticles as a multifunctional material nanoplatform has great potential for a variety of advanced biomedical applications.

2 Experimental

2.1 Synthesis of Fe_2O_3@PF nanoparticles

$Fe(NO_3)_3 \cdot 9H_2O$, N,N-dimethylformamide (DMF), ethanol (99.7%), hexamethylenetetramine (HMT), tetraethoxysilane (TEOS), phenol, ammonia, and cetyltrimethylammoniumbromide (CTAB) of analysis grade were purchased from Sinopharm Chemical Reagent Co., Ltd. Poly(N-vinyl-2-pyrrolidone) (PVP K30) of analysis grade was obtained from Tianjin Kermel Chemical Reagent. All chemicals were used as received. Quasicubic α-Fe_2O_3 nanoparticles were prepared via a modified solvothermal method [37]. In a typical experiment, 1.212 g of $Fe(NO_3)_3 \cdot 9H_2O$ and 1.8 g of PVP K30 were dissolved in 108 mL of DMF. The solution was then poured into a Teflon-lined stainless steel autoclave and heated at 180 °C for 30 h. After the reaction, a red precipitate was collected by centrifugation, washed with deionized water and ethanol several times, and then redispersed in water. Then, the as-prepared Fe_2O_3 (50 mg) nanoparticles were dispersed well in 120 mL of water by ultrasonication for 10 min, and subsequently a mixture of 3 mmol phenol (99%) and 1.5 mmol HMT aqueous solution

was added. After ultrasonication for another 10 min, the solution was transferred into a Teflon-lined autoclave, heated to 160 ℃, and maintained at that temperature for 4 h. Orange Fe_2O_3 coated with a layer of phenol-formaldehyde resin (Fe_2O_3@PF) was collected by centrifugation, and washed with deionized water several times. The Fe_2O_3@PF was then dispersed in water for later use.

2.2 Synthesis of Fe_2O_3@PF@mSiO_2 nanoparticles

Silica shells were grown on the Fe_2O_3@PF sphere surfaces by a modified Stöber process in the presence of CTAB at 30 ℃. Typically, 0.16 g of CTAB was stirred with 5 mL of deionized water for 1 h with a magnetic stir bar. This solution was then added to a mixture of 50 mg Fe_2O_3@PF, 25 mL deionized water, 10 mL ethanol, and 0.4 mL ammonia solution (28%–30%). The mixture was stirred for 30 min before the dropwise addition of 0.28 mL TEOS over a short period. The reaction was left to proceed at 30 ℃ for 16 h. Finally, Fe_2O_3@PF@mSiO_2 was collected by centrifugation, sequentially washed with deionized water and ethanol, and dried in air at 50 ℃ for 24 h.

2.3 Synthesis of Fe_3O_4@C nanoparticles

The synthesis of Fe_3O_4@C nanoparticles involves two steps: pyrolysis and removal of the silica shell. First, the Fe_2O_3@PF@mSiO_2 was heated at 5 ℃·min^{-1} to 150 ℃, and held at this temperature for 1 h. The temperature was then increased to 600 ℃ at a heating rate of 5 ℃·min^{-1} and maintained at that temperature for 2 h. Dissolution of the silica shell was then performed using an NaOH–alcohol–water solution (1.875 M) at 50 ℃ for 24 h to generate the Fe_3O_4@C nanospheres.

2.4 Characterization

Transmission electron microscope (TEM) images were obtained with a Tecnai G220 S-Twin microscope at an acceleration voltage of 200 kV. Scanning electron microscope (SEM) images were obtained with a FEI Nova NanoSEM 450 instrument. X-ray diffraction (XRD) patterns were obtained with a Rigaku D/MAX-2400 diffractometer using Cu Kα radiation (40 kV, 100 mA, λ = 1.54056 Å). Mössbauer measurements were performed to determine the phase composition in the Fe_3O_4@C sample using an electrodynamic spectrometer with a 57Co/Rh γ-ray source. The spectra were obtained at room temperature and fitted using the MossWinn fitting package. Thermogravimetric and differential scanning calorimetry analyses (TG-DSC) were conducted on a thermogravimetric analyzer STA 449 F3 Jupiter (NETZSCH), in air with a heating rate of 10 ℃·min^{-1}. Nitrogen sorption isotherms were measured with an ASAP 2020 adsorption analyzer (Micromeritics) at the temperature of liquid nitrogen. A vibrating magnetometer (MPMS (SQUID) XL-7, Quantum Design) was used to study the magnetic properties, with an applied magnetic field of –2.0–2.0 T at 298 K. The powdered sample was immobilized in a hard gelatin capsule during the measurement.

2.5 *In vitro* biocompatibility assays

Cell viability was determined using a Cell Counting Kit-8 (CCK-8, Dojindo Laboratories in Japan). First, 8000 MCF-7 (human breast adenocarcinoma) cells were seeded into 96-well microplates (Costar, Corning, NY) and grown in a medium containing 1640/RIPM medium, fetal bovine serum (FBS, 10% (*v*/*v*)), penicillin (100 U·mL^{-1}), streptomycin (100 μg·mL^{-1}), and L-glutamine (2 mM) at 37 ℃ for 24 h. Different concentrations of Fe_3O_4@C were added to the complete medium to test their influence on the viability of the MCF-7 cells after exposure for 24 h. Cell viability was calculated as the ratio of the absorbance of test cells to that of untreated cells. Absorbance was measured at 450 nm with a reference at 600 nm using an Infinite M200 microplate reader (Tecan, Durham, NC, USA).

2.6 MRI *in vitro*

The relaxivity measurements were performed on a 7.0 T clinical MRI instrument (Bruker BioSpec 70/20 USR). An extremity coil was used for the data acquisition, and the pulse sequence used was a T_2-weighted turbo spin-echo sequence with the following parameters: repetition time (TR) = 3,000 ms, echo time (TE) = 20 ms, slice thickness = 1 mm, field of view (FOV) = 30 × 30 mm, number of acquisitions = 1.

2.7 MRI *in vivo*

In vivo T_2-weighted MRI images were recorded on a

GE HDxt 3.0 T MRI scanner before and at different times after injection of the magnetic samples. Sprague Dawley (SD) rats were anesthetized with chloral hydrate, and then contrast agents were administered by tail vein injection after the rats stabilized. Typically, nanoparticles suspended in 5% (*w*/*v*) glucose injection (~1 mL) were administered to SD rats (6–8 weeks of age, body mass ~275 ± 25 mg) through tail vein injection at a dose of 0.84 mg Fe per kg body weight. The dosage was calculated based on the metal concentration. MRI was performed immediately after injection at 1.5, 3, 5, 12, and 30 h (n = 6 rats per group). The scanning parameters used were similar to those used for the *in vitro* MRI imaging except for different TE and TR. The TE and TR of the T_2-weighted images were 86.1 and 2,620 ms, respectively. All animal operations were conducted in accordance with the People's Republic of China (PRC) national standards for laboratory animal quality, and the Chinese guideline for the care and use of laboratory animals. No abnormalities were observed after the injection of any rats.

2.8 Laser irradiation

To obtain the temperature curve, the Fe_3O_4@C solution was added to a 96-well microplate and then irradiated by laser with a power density of 6.5 W·cm^{-2} at regular intervals. Meanwhile, a thermocouple detector was immersed in the solution and left to measure the temperature. MCF-7 cells were seeded into 60 mm petri dishes and incubated with Fe_3O_4@C (100 μg·mL^{-1}) in complete medium for 24 h. The cells were detached from the dishes with trypsin containing EDTA and collected as a pellet (about 1 × 10^6 cells/pellet within 0.5 mL complete medium) at the bottom of an EP vial. Cells were placed in an incubator at 37 ˚C throughout the entire irradiation procedure. The femtosecond pulsed laser (at 750 nm) had a spot of 2 mm diameter, and the power could be tuned to attain the desired power density (laser power/spot area) (Spectra Physics).

2.9 Live-dead assay

Under different concentrations of Fe_3O_4@C, MCF-7 cells were irradiated by a laser and the Live-dead assay was used to assess the influence of culture time on cell death. Cells in live or dead states were stained different colors. Live cells show green fluorescence due to staining with calcein, and dead cells exhibit red fluorescence because ethidium homodimer can penetrate the impaired membrane and stain the nucleus. The ratio of dead to live cells was then analyzed to assess the thermal effects.

3 Results and discussion

The synthesis of carbon-protected magnetic nanoparticles is illustrated in Fig. 1. As a proof of concept, colloidal Fe_2O_3 nanoparticles of 40 nm (Fig. 1(b)) were chosen as core materials, and were produced through a facile solvothermal method [37]. The zeta potential analysis (see Fig. S1 in Electronic Supplementary

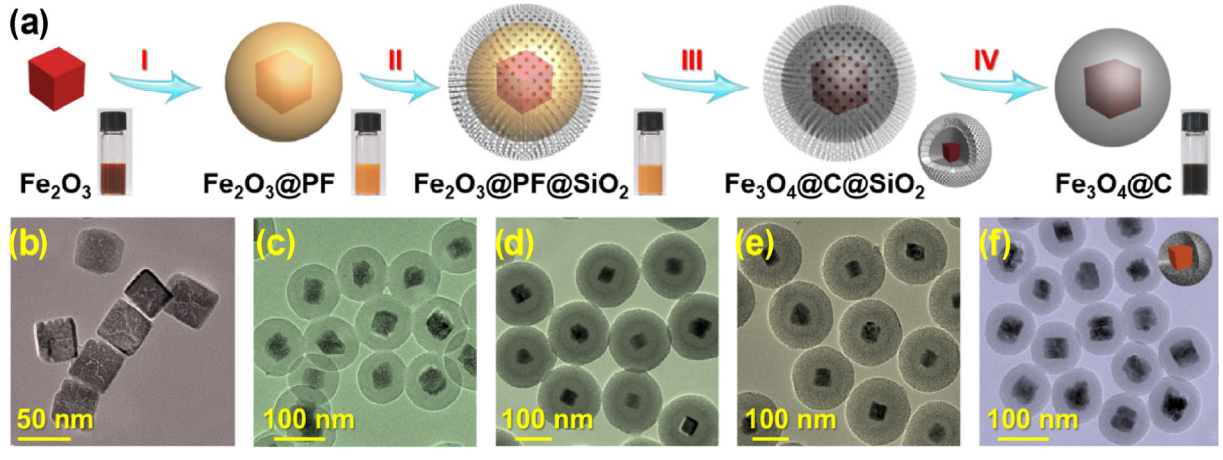

Figure 1 Synthesis and TEM analyses of the products obtained from each step. (a) Schematic illustration of the sequentially designed surface by the nano-engineering process: I, polymer encapsulation; II, silica coating; III, confined nanospace pyrolysis; IV, silica removal. TEM analyses of (b) Fe_2O_3, (c) Fe_2O_3@PF, (d) Fe_2O_3@PF@SiO_2, (e) Fe_3O_4@C@SiO_2, and (f) Fe_3O_4@C.

Material (ESM)) indicates that the Fe_2O_3 nanoparticles can form homogeneous suspensions in an aqueous solution (pH ~ 7.5) consisting of phenol and HMT. This allows the formation of a uniform polymer coating (which later serves as the carbon precursor) on individual Fe_2O_3 nanoparticles (denoted Fe_2O_3@PF, diameter ~100 nm, Fig. 1(c)) by a hydrothermal reaction. Direct thermal annealing would result in coalescence of the polymer shells, and therefore a uniform protecting silica shell, thus creating a confined space for pyrolysis. The shell is coated onto the Fe_2O_3@PF by using a modified Stöber method to obtain Fe_2O_3@PF@SiO_2 nanospheres (Fig. 1(d)). After pyrolysis, the polymer shell is carbonized, and the Fe_2O_3 core is carbothermally reduced to Fe_3O_4; thus, a single-core, double-shell nanostructure, Fe_3O_4@C@SiO_2, is obtained (Fig. 1(e)).

Finally, the silica is leached and individual Fe_3O_4 nanocubes are present in a porous carbon shell in the form of Fe_3O_4@C nanoparticles with a mean size of ~90 nm, as indicated in the TEM images (Fig. 1(f)). Such nanoparticles can form a colloidal suspension in water without the need for surfactants. Furthermore, the nanoparticles can be attracted by an external magnet (see Fig. S2 in the ESM). It should be noted that the silica coating is an indispensable step to achieve discrete carbon-protected magnetic nanoparticles; otherwise, the sticky polymer shells agglomerate during thermal treatment. The intact silica shell creates a nanoreactor in which the phenolic resin is confined and converted into carbon [36]. Furthermore, the thickness of the polymer shell can be tuned from around 4 to 80 nm, depending on the amount of polymer precursor used (see Fig. S3 in the ESM). This in turn means that the thickness of the carbon shell and the overall size of the carbon-protected magnetic nanoparticles are adjustable and can be tailored to the requirements of a specific application. It is also important to note that the carbon shell efficiently prevents sintering of the nanosized metal core and simultaneously renders them functional for photothermal effects and loading with drug molecules [38].

As observed from the SEM images in Fig. 2(a) and Fig. S4 (in the ESM), the obtained Fe_3O_4@C sample is composed of uniform nanoparticles with a size of ~90 nm. The dynamic light scattering (DLS) measurement in Fig. 2(b) confirms a uniform particle size of 140 nm (hydrodynamic diameter) with a polydispersity

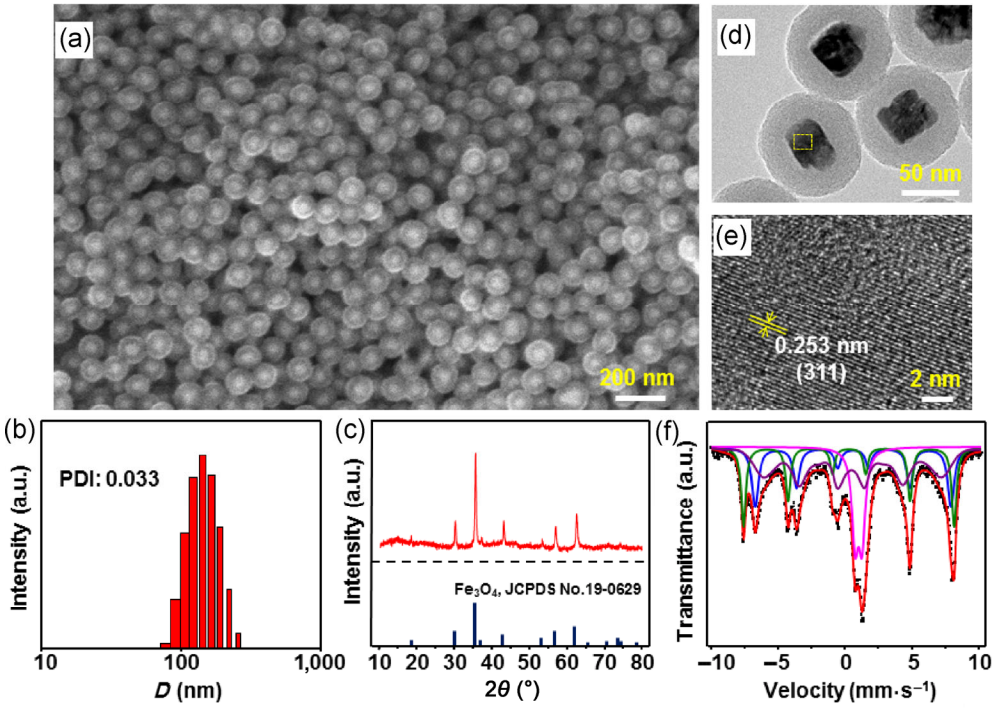

Figure 2 Characterization of carbon-protected magnetic nanoparticles. (a) SEM image. (b) DLS measurement. (c) XRD pattern. (d) TEM image. (e) HRTEM image of the selected area in (d). (f) Mössbauer spectrum of carbon-protected magnetic nanoparticles.

index (PDI) of 0.033, suggesting that the nanoparticles are monodisperse in water without clustering or aggregation.

The XRD pattern of the sample (Fig. 2(c)) matches well with that of the magnetite Fe_3O_4 phase (JCPDS No. 19-0629). In Fig. 2(d), the TEM image of Fe_3O_4@C shows that the iron oxide nanoparticle is tightly encapsulated by an amorphous carbon shell. Uniform lattice fringes with a spacing corresponding to Fe_3O_4 (311) are observed in the high-resolution TEM (HRTEM) image of the selected area (Fig. 2(e)). Using the Scherrer equation, the average crystallite size of Fe_3O_4 is estimated, from the peak width of Fe_3O_4 (311) and Fe_3O_4 (440), to be 18.6 ± 1.4 nm, i.e., much smaller than the particle sizes observed by TEM. Obviously, this synthesis leads to fragmentation of the iron oxide nanoparticles into smaller crystalline domains due to the carbothermal reduction of α-Fe_2O_3 to Fe_3O_4 by partially eliminating lattice oxygen during the phase transformation. Further, the phase composition of the iron oxide core is confirmed by Mössbauer spectroscopy (Fig. 2(f) and Table S1 in the ESM). It can be deduced from the hyperfine parameters that the iron oxide core is predominantly composed of Fe_3O_4 nanoparticles with a relaxing component that displays a superparamagnetic relaxation at room temperature [39]. The Brunauer-Emmett-Teller (BET) equivalent specific surface area of Fe_3O_4@C, as analyzed by N_2 sorption (see Fig. S5 in the ESM), is 502 $m^2 \cdot g^{-1}$. The oxidation resistance of Fe_3O_4@C was monitored by TG analysis in air (see Fig. S5 in the ESM). The mass of Fe_3O_4@C remains constant up to 400 °C, indicating that below that temperature the carbon coating is quite stable against oxidation.

Figure 3(a) shows that the absolute zeta potential value is above 30 mV in the pH range of 5–11, indicating that these nanoparticles can be stably dispersed in an aqueous solution, affording a black colloidal solution (Fig. 3(a), inset). The obtained solution can completely pass through the 0.22-μm membrane filter after one month of storage without the addition of surfactants, confirming the complete absence of aggregation. Magnetization of Fe_3O_4@C at 298 K is measured to be 90 $emu \cdot g^{-1}$, where the magnetization value is normalized to the Fe_3O_4 content (Fig. 3(b)). After one year of storage under ambient conditions, the magnetic

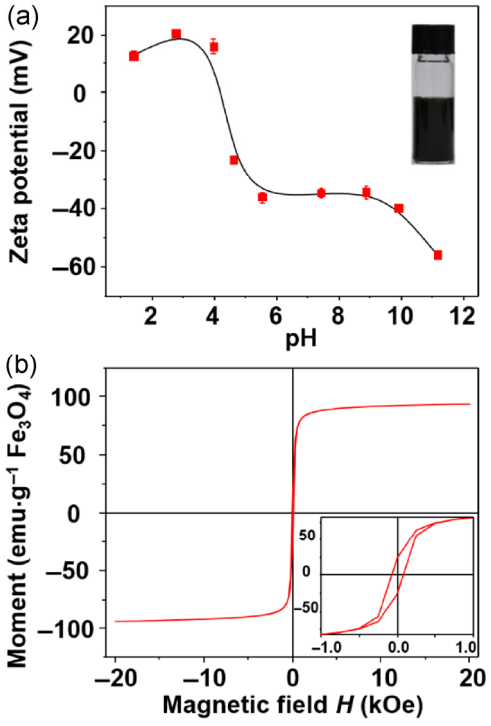

Figure 3 (a) Zeta potential (inset: photograph of high colloidal stability of magnetic nanoparticles in water). (b) Room temperature magnetization (M) versus field (H) measured at 298 K (inset: M–H curve in the low-field region area), the magnetization, coercivity (H_c), and remanent magnetization (M_r) are ~90 $emu \cdot g^{-1}$, 81 Oe, and 25 $emu \cdot g^{-1}$ (Fe_3O_4), respectively, as determined by a superconducting quantum interference device magnetometer (SQUID).

response of the sample was rechecked, with no obvious degradation observed (see Fig. S6 in the ESM), indicating that the magnetic core is well protected by the carbon shell. This value enables use of these nanoparticles for many biomedical applications (i.e., MRI contrast enhancement and biological separation). To the best of our knowledge, this is the first report on the synthesis of such uniform, discrete, and colloidal carbon-protected magnetic nanoparticles.

Because the as-prepared nanoparticles are water-dispersible and discrete, the colloidal nanoparticles can be used directly as an MRI contrast agent, thus avoiding complex procedures of further modification or transfer [40]. We measured the transverse relaxivity of the sample by a 7.0 T MR scanner. The T_2 relaxivity coefficient (r_2) is 384 $mM^{-1} \cdot S^{-1}$ (Fig. 4(a)), which is greater than or equal to that of commercially available superparamagnetic iron oxide nanoparticles (Feridex, Bayer HealthCare Pharmaceuticals) as well as other

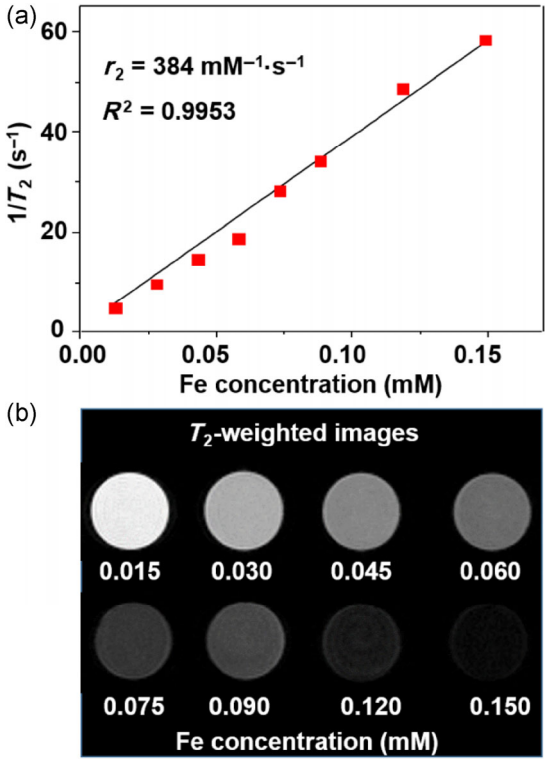

Figure 4 *In vitro* MRI measurement. (a) T_2 relaxivity plot of an aqueous suspension of Fe_3O_4@C measured at 7.0 T, the slope indicates the T_2 relaxivity coefficient (r_2). (b) T_2-weighted MR images of Fe_3O_4@C nanoparticles suspended in water at different Fe concentrations.

magnetic nanoparticles reported in the literature [41]. With the increase in the Fe concentration, the signal intensity of T_2-weighted phantom images obviously decrease (Fig. 4(b)), indicating that such nanoparticles have the potential to generate MRI contrast enhancement on T_2-weighted sequences.

To use colloidal Fe_3O_4@C in biological applications, it must be non-toxic. Before the animal study, we first tested its cytotoxicity by using the human breast adenocarcinoma MCF-7 cell line as a model. The CCK-8 viability assay indicates that the obtained nanoparticles have no appreciable cytotoxicity for 24 h, even at a concentration of 120 μg Fe_3O_4@C per mL (25 μg Fe per mL), suggesting the high biocompatibility of the carbon-protected magnetic nanoparticles (see Fig. S7 in the ESM). This is strong confirmation that the carbon shell is biocompatible. Encouraged by the high colloidal stability, uniform nanosize, high relaxivity, and the biocompatibility of our carbon-protected magnetic nanoparticles, they were used as contrast agents for preliminary *in vivo* MRI in rats.

The *in vivo* contrast-enhancing effect of Fe_3O_4@C was evaluated in rats by injection of Fe_3O_4@C dispersed in a 5% (*w*/*v*) glucose solution at a dose of 0.84 mg Fe per kg of rat body weight (10% of that typically used for existing Gd agents). A time sequence of images was taken from 1.5 to 30 h after intravenous injection. The magnetic resonance signal intensity of the liver parenchyma (Fig. 5) and kidney (see Fig. S7 in the ESM) in the T_2-weighted sequences changes with time, which is possible due to the ultrahigh r_2 relaxivity of Fe_3O_4@C nanoparticles. These results achieve a major goal of MRI contrast-agent development, i.e., long-circulating contrast enhancement at low metal dosages *in vivo*, which will facilitate MRI and other applications.

Taking advantage of the light-absorbing property and the high surface area of the Fe_3O_4@C nanoparticles, as well as the excellent bioimaging properties, the materials were examined for photothermal therapy under laser irradiation (see Figs. S7 and S8 in the ESM). At a low Fe_3O_4@C concentration (50 μg·mL^{-1}), photothermal heating occurs upon λ = 750 nm laser irradiation. At high concentrations (up to 200 μg·mL^{-1}),

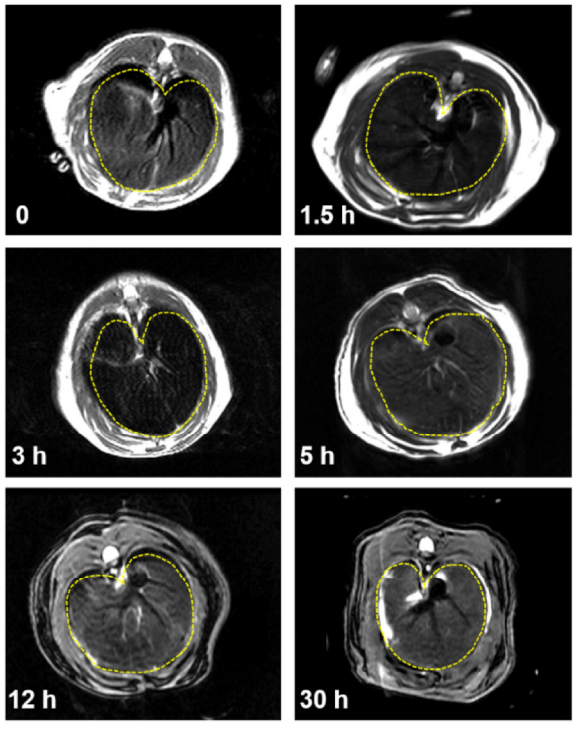

Figure 5 *In vivo* T_2-weighted MRI images of liver before and after intravenous administration of 0.84 mg Fe per kg body weight of Fe_3O_4@C hybrids (after 0, 1.5, 3, 5, 12, and 30 h).

the temperature can reach values as high as 70 ˚C in 10 min under 750 nm laser irradiation, which is an extremely high photothermal heating effect. The photothermal conversion efficiency (η) of Fe_3O_4@C is 21.7% (Fig. S8 in the ESM), which was measured according to the reported method (see the ESM for the detailed calculations) [42, 43]. Then, MCF-7 cells were incubated with the Fe_3O_4@C nanoparticles for 24 h using a concentration of 100 μg·mL^{-1}. After rinsing with a PBS buffer, the cells were irradiated by a 750 nm femtosecond laser at regular intervals (see Fig. S9 in the ESM). Without Fe_3O_4@C nanoparticles, no photothermal effect is noticed, even after irradiation for 15 min. After adding nanoparticles, the photothermal ability goes into effect after 5 min of irradiation and about 10% of the MCF-7 cells are killed. More efficient tumoricidal potential is observed when the mixture is irradiated for 15 min, after which nearly 50% of the MCF-7 cells are killed. The excellent thermal generation of the Fe_3O_4@C nanoparticles under laser irradiation demonstrates the potential for photothermal therapy using the sample. Overall, the obtained carbon-protected magnetic nanoparticles have great potential for simultaneous bioimaging, diagnosis, and therapy. To the best of our knowledge, there is so far no other report on the synthesis of such colloidal carbon-protected iron oxides nanoparticles, which are promising for biomedical applications.

4 Conclusions

In summary, a novel nano-engineering approach is developed for the preparation of core–shell structured carbon-protected magnetic nanoparticles that are discrete, uniform, water-dispersible, and biocompatible. The precise integration of carbon coatings with magnetic monodispersed nanoparticles is used to form a uniform core–shell hybrid that monodisperses in water without clustering or aggregation while possessing high biocompatibility. The particles can be used for imaging and the treatment of resistant cancers by combining their different functions, including MRI enhancement, photothermal therapy, and high surface-to-volume ratio. Thus, a unique and versatile material platform is provided, which is essential and crucial for future advanced applications.

Acknowledgements

This project was financially supported by National Natural Science Foundation of China (No. 21225312). We appreciate Dr. Fang Fang at Wuhan Institute of Physics and Mathematics of China for assistance with the *in vitro* MRI measurement, Dr. Liming Wang at National Center for Nanoscience and Technology of China for assistance with the cell experiments.

Electronic Supplementary Material: Supplementary material (further details of SEM, TEM images, N_2 sorption isotherms, fluorescence microscope images, etc.) is available in the online version of this article at http://dx.doi.org/10.1007/s12274-016-1042-9.

References

[1] Mahmoudi, M.; Hosseinkhani, H.; Hosseinkhani, M.; Boutry, S.; Simchi, A.; Journeay, W. S.; Subramani, K.; Laurent, S. Magnetic resonance imaging tracking of stem cells *in vivo* using iron oxide nanoparticles as a tool for the advancement of clinical regenerative medicine. *Chem. Rev.* **2011**, *111*, 253–280.

[2] Lu, A.-H.; Salabas, E. L.; Schüth, F. Magnetic nanoparticles: Synthesis, protection, functionalization, and application. *Angew. Chem., Int. Ed.* **2007**, *46*, 1222−1244.

[3] Gallo, J.; Long, N. J.; Aboagye, E. O. Magnetic nanoparticles as contrast agents in the diagnosis and treatment of cancer. *Chem. Soc. Rev.* **2013**, *42*, 7816−7833.

[4] Caravan, P.; Ellison, J. J.; McMurry, T. J.; Lauffer R. B. Gadolinium(III) chelates as MRI contrast agents: Structure, dynamics and applications. *Chem. Rev.* **1999**, *99*, 2293–2352.

[5] Wang, C.; Chen, J. C.; Zhou, X. R.; Li, W.; Liu, Y.; Yue, Q.; Xue, Z. T.; Li, Y. H.; Elzatahry, A. A.; Deng, Y. H. et al. Magnetic yolk–shell structured anatase-based microspheres loaded with Au nanoparticles for heterogeneous catalysis. *Nano Res.* **2015**, *8*, 238–245.

[6] Ananta, J. S.; Godin, B.; Sethi, R.; Moriggi, L.; Liu, X. W.; Serda R. E.; Krishnamurthy, R.; Muthupillai, R.; Bolskar, R. D.; Helm, L. et al. Geometrical confinement of gadolinium-based contrast agents in nanoporous particles enhances T_1 contrast. *Nat. Nanotechnol.* **2010**, *5*, 815–821.

[7] Piao, Y. Z.; Kim, J.; Na, H. B.; Kim, D.; Baek, J. S.; Ko, M. K.; Lee, J. H.; Shokouhimehr, M.; Hyeon, T. Wrap-bake-peel process for nanostructural transformation from β-FeOOH nanorods to biocompatible iron oxide nanocapsules. *Nat. Mater.* **2008**, *7*, 242−247.

[8] Colombo, M.; Carregal-Romero, S.; Casula, M. F.; Gutiérrez, L.; Morales, M. P.; Böhm, I. B.; Heverhagen, J. T.; Prosperi, D.; Parak, W. J. Biological applications of magnetic nanoparticles. *Chem. Soc. Rev.* **2012**, *41*, 4306−4334.

[9] Ma, X. X.; Tao, H. Q.; Yang, K.; Feng, L. Z.; Cheng, L.; Shi, X. Z.; Li, Y. G.; Guo, L.; Liu Z. A functionalized graphene oxide–iron oxide nanocomposite for magnetically targeted drug delivery, photothermal therapy, and magnetic resonance imaging. *Nano Res.* **2012**, *5*, 199–212.

[10] Huang, Y. M.; Hu, L.; Zhang, T. T.; Zhong, H.; Zhou, J. J.; Liu, Z. B.; Wang, H. B.; Guo, Z.; Chen, Q. W. $Mn_3[Co(CN)_6]_2$@SiO_2 core–shell nanocubes: Novel bimodal contrast agents for MRI and optical imaging. *Sci. Rep.* **2013**, *3*, 2647.

[11] Sun, Z. K.; Yang, J. P.; Wang, J. X.; Li, W.; Kaliaguine, S.; Hou, X. F.; Deng, Y. H.; Zhao, D. Y. A versatile designed synthesis of magnetically separable nano-catalysts with well-defined core–shell nanostructures. *J. Mater. Chem. A* **2014**, *2*, 6071–6074.

[12] Zhou, L.; Li, Z. H.; Ju, E. G.; Liu, Z.; Ren, J. S.; Qu, X. G. Aptamer-directed synthesis of multifunctional lanthanide-doped porous nanoprobes for targeted imaging and drug delivery. *Small* **2013**, *9*, 4262−4268.

[13] Jun, Y. W.; Lee, J.-H.; Cheon, J. Chemical design of nanoparticle probes for high performance magnetic resonance imaging. *Angew. Chem., Int. Ed.* **2008**, *47*, 5122–5135.

[14] Shah, B.; Yin, P. T.; Ghoshal, S.; Lee, K. B. Multimodal magnetic core–shell nanoparticles for effective stem-cell differentiation and imaging. *Angew. Chem., Int. Ed.* **2013**, *52*, 6190–6195.

[15] Laurent, S.; Forge, D.; Port, M.; Roch, A.; Robic, C.; Vander Elst, L.; Muller, R. N. Magnetic iron oxide nanoparticles: Synthesis, stabilization, vectorization, physicochemical characterizations, and biological applications. *Chem. Rev.* **2008**, *108*, 2064–2110.

[16] Reddy, L. H.; Arias, J. L.; Nicolas, J.; Couvreur, P. Magnetic nanoparticles: Design and characterization, toxicity and biocompatibility, pharmaceutical and biomedical applications. *Chem. Rev.* **2012**, *112*, 5818−5878.

[17] Xia, A.; Hu, J. H.; Wang, C. C.; Jiang, D. L. Synthesis of magnetic microspheres with controllable structure via polymerization-triggered self-positioning of nanocrystals. *Small* **2007**, *3*, 1811−1817.

[18] Wang, Y.; Teng, X. W.; Wang, J. S.; Yang, H. Solvent-free atom transfer radical polymerization in the synthesis of Fe_2O_3@polystyrene core–shell nanoparticles. *Nano Lett.* **2003**, *3*, 789−793.

[19] Xu, Z. Z.; Wang, C. C.; Yang, W. L.; Deng, Y. H.; Fu, S. K. Encapsulation of nanosized magnetic iron oxide by polyacrylamide via inverse miniemulsion polymerization. *J. Magn. Magn. Mater.* **2004**, *277*, 136–143.

[20] Xu, H.; Cui, L. L.; Tong, N. H.; Gu, H. C. Development of high magnetization Fe_3O_4/polystyrene/silica nanospheres via combined miniemulsion/emulsion polymerization. *J. Am. Chem. Soc.* **2006**, *128*, 15582–15583.

[21] Zeng, J. F.; Jing, L. H.; Hou, Y.; Jiao, M. X.; Qiao, R. R.; Jia, Q. J.; Liu, C. Y.; Fang, F.; Lei, H.; Gao, M. Y. Anchoring group effects of surface ligands on magnetic properties of Fe_3O_4 nanoparticles: Towards high performance MRI contrast agents. *Adv. Mater.* **2014**, *26*, 2694–2698.

[22] Lu, Y.; Yin, Y. D.; Mayers, B. T.; Xia, Y. N. Modifying the surface properties of superparamagnetic iron oxide nanoparticles through a sol-gel approach. *Nano Lett.* **2002**, *2*, 183−186.

[23] Deng, Y. H.; Qi, D. W.; Deng, C. H.; Zhang, X. M.; Zhao, D. Y. Superparamagnetic high-magnetization microspheres with an Fe_3O_4@SiO_2 core and perpendicularly aligned mesoporous SiO_2 shell for removal of microcystins. *J. Am. Chem. Soc.* **2008**, *130*, 28−29.

[24] Ge, J. P.; Hu, Y. X.; Zhang, T. R.; Yin, Y. D. Superparamagnetic composite colloids with anisotropic structures. *J. Am. Chem. Soc.* **2007**, *129*, 8974−8945.

[25] Yue, Q.; Zhang, Y.; Wang, C.; Wang, X. Q.; Sun, Z. K.; Hou, X. F.; Zhao, D. Y.; Deng, Y. H. Magnetic yolk–shell mesoporous silica microspheres with supported Au nanoparticles as recyclable high-performance nanocatalysts. *J. Mater. Chem. A* **2015**, *3*, 4586–4594.

[26] Yue, Q.; Li, J. L.; Luo, W.; Zhang, Y.; Elzatahry, A. A.; Wang, X. Q.; Wang, C.; Li, W.; Cheng, X. W.; Alghamdi, A. et al. An interface coassembly in biliquid phase: Toward core–shell magnetic mesoporous silica microspheres with tunable pore size. *J. Am. Chem. Soc.* **2015**, *137*, 13282–13289.

[27] Xuan, S. H.; Hao, L. Y.; Jiang, W. Q.; Gong, X. L.; Hu, Y.; Chen, Z. Y. A facile method to fabricate carbon-encapsulated Fe_3O_4 core/shell composites. *Nanotechnology* **2007**, *18*, 035602.

[28] Zhang, X. B.; Tong, H. W.; Liu, S. M.; Yong, G. P.; Guan, Y. F. An improved stöber method towards uniform and monodisperse Fe_3O_4@C nanospheres. *J. Mater. Chem. A* **2013**, *1*, 7488−7493.

[29] Du, Y. C.; Liu, W. W.; Qiang, R.; Wang, Y.; Han, X. J.; Ma, J.; Xu, P. Shell thickness-dependent microwave absorption of core–shell Fe_3O_4@C composites. *ACS Appl. Mater. Interfaces* **2014**, *6*, 12997−13006.

[30] Kim, J.; Kim, H. S.; Lee, N.; Kim, T.; Kim, H.; Yu, T.; Song, I. C.; Moon, W. K.; Hyeon, T. Multifunctional uniform nanoparticles composed of a magnetite nanocrystal core and a mesoporous silica shell for magnetic resonance and fluorescence imaging and for drug delivery. *Angew. Chem., Int. Ed*. **2008**, *47*, 8438−8441.

[31] Lu, A.-H.; Hao, G.-P.; Sun, Q.; Zhang, X.-Q.; Li, W.-C. Chemical synthesis of carbon materials with intriguing nanostructure and morphology. *Macromol. Chem. Phys.* **2012**, *213*, 1107–1131.

[32] Fang, Y.; Gu, D.; Zou, Y.; Wu, Z. X.; Li, F. Y.; Che, R. C.; Deng, Y. H.; Tu, B.; Zhao, D. Y. A low-concentration hydrothermal synthesis of biocompatible ordered mesoporous carbon nanospheres with tunable and uniform size. *Angew. Chem., Int. Ed.* **2010**, *49*, 7987–7991.

[33] Zhang, G. Q.; Wu, H. B.; Song, T.; Paik, U.; Lou, X. W. TiO_2 hollow spheres composed of highly crystalline nanocrystals exhibit superior lithium storage properties. *Angew. Chem., Int. Ed.* **2014**, *53*, 12590–12593.

[34] Gu, L.; Koymen, A. R.; Mohanty, S. K. Crystalline magnetic carbon nanoparticle assisted photothermal delivery into cells using CW near-infrared laser beam. *Sci. Rep.* **2014**, *4*, 5106.

[35] Yu, G. B.; Sun, B.; Pei, Y.; Xie, S. H.; Yan, S. R.; Qiao, M. H.; Fan, K. N.; Zhang, X. X.; Zong, B. N. Fe_xO_y@C spheres as an excellent catalyst for Fischer–Tropsch synthesis. *J. Am. Chem. Soc.* **2010**, *132*, 935–937.

[36] Lu, A.-H.; Sun, T.; Li, W.-C.; Sun, Q.; Han, F.; Liu, D.-H.; Guo, Y. Synthesis of discrete and dispersible hollow carbon nanospheres with high uniformity by using confined nanospace pyrolysis. *Angew. Chem., Int. Ed.* **2011**, *50*, 11765−11768.

[37] Zheng, Y. H.; Cheng, Y.; Wang, Y. S.; Bao, F.; Zhou, L. H.; Wei, X. F.; Zhang, Y. Y.; Zheng, Q. Quasicubic α-Fe_2O_3 nanoparticles with excellent catalytic performance. *J. Phys. Chem. B* **2006**, *110*, 3093−3097.

[38] Wang, L. M.; Sun, Q.; Wang, X.; Wen, T.; Yin, J.-J.; Wang, P. Y.; Bai, R.; Zhang, X.-Q.; Zhang, L.-H.; Lu, A.-H. et al. Using hollow carbon nanospheres as a light-induced free radical generator to overcome chemotherapy resistance. *J. Am. Chem. Soc.* **2015**, *137*, 1947−1955.

[39] Murad, E. Magnetic properties of microcrystalline iron (III) oxides and related materials as reflected in their Mössbauer spectra. *Phys. Chem. Minerals* **1996**, *23*, 248−262.

[40] Zhao, Z. H.; Zhou, Z. J.; Bao, J. F.; Wang, Z. Y.; Hu, J.; Chi, X. Q.; Ni, K. Y.; Wang, R. F.; Chen, X. Y.; Chen, Z. et al. Octapod iron oxide nanoparticles as high-performance T_2 contrast agents for magnetic resonance imaging. *Nat. Commun.* **2013**, *4*, 2266.

[41] Seo, W. S.; Lee, J. H.; Sun, X. M.; Suzuki, Y.; Mann, D.; Liu, Z.; Terashima, M.; Yang, P. C.; McConnell, M. V.; Nishimura, D. G. et al. FeCo/graphitic-shell nanocrystals as advanced magnetic-resonance-imaging and near-infrared agents. *Nat. Mater.* **2006**, *5*, 971−976.

[42] Tian, Q. W.; Jiang, F. R.; Zou, R. J.; Liu, Q.; Chen, Z. G.; Zhu, M. F.; Yang, S. P.; Wang, J. L.; Wang, J. H.; Hu, J. Q. Hydrophilic Cu_9S_5 nanocrystals: A photothermal agent with a 25.7% heat conversion efficiency for photothermal ablation of cancer cells *in vivo*. *ACS Nano* **2011**, *5*, 9761–9771.

[43] Liu, J.; Zheng, X. P.; Yan, L.; Zhou, L. J.; Tian, G.; Yin, W. Y.; Wang, L. M.; Liu, Y.; Hu, Z. B.; Gu, Z. J. et al. Bismuth sulfide nanorods as a precision nanomedicine for *in vivo* multimodal imaging-guided photothermal therapy of tumor. *ACS Nano* **2015**, *9*, 696–707.